the subducted lithosphere temperature, and thus its age.

Although in our experiments the absolute stress value remains high (fig. S2B) compared with stresses expected within the cold core of subducted slabs (25), the observed stress drops are broadly consistent with those calculated for deep earthquakes (1, 18, 20, 21). Constant differential stress conditions at failure over a wide range of confinement (2 to 5 GPa) strongly suggest that transformational faulting is largely independent of normal stress and thus involves nonfrictional processes. We suggest that rupture nucleation is controlled by dislocation density and spinel nucleation kinetics, whereas propagation is controlled by superplastic flow. High-stress and high–dislocation density conditions can be met in a cold subducting slab full of metastable olivine (26–28) owing to stress concentrations at the micro- and mesoscopic scales because of buckling, folding, and/or inherited fractures (29). This is particularly true in the Tonga-Kermadec region, for instance (28, 29), for which the largest catalog of deep-focus earthquakes is available (1).

References and Notes

1. C. Frohlich, *Deep Earthquakes* (Cambridge Univ. Press, Cambridge, 2006).
2. J. D. Byerlee, *Pure Appl. Geophys.* **116**, 586–602 (1978).
3. C. Marone, *Annu. Rev. Earth Planet. Sci.* **26**, 643–696 (1998).
4. M. S. Paterson, T.-f. Wong, *Experimental Rock Deformation—The Brittle Field*. (Springer–Verlag, Berlin, Heidelberg, 2005).
5. D. T. Griggs, D. W. Baker, *The Origin of Deep-Focus Earthquakes*, H. Mark, S. Fernbach, Eds. (Interscience, New York, 1969), pp. 23–42.
6. S. Kirby, *J. Geophys. Res.* **92**, 13789–13800 (1987).
7. H. W. Green II, P. C. Burnley, *Nature* **341**, 733–737 (1989).
8. P. C. Burnley, H. W. Green II, D. Prior, *J. Geophys. Res.* **96**, (B1), 425–443 (1991).
9. H. W. Green II, T. E. Young, D. Walker, C. H. Scholz, *Nature* **348**, 720–722 (1990).
10. H. W. Green II, C. H. Scholz, T. N. Tingle, T. E. Young, T. A. Koczinski, *Geophys. Res. Lett.* **19**, 789–792 (1992).
11. E. M. Riggs, H. W. Green II, *J. Geophys. Res.* **110**, B03202 (2005).
12. Materials and methods are available as supplementary materials on *Science* Online.
13. N. Hilairet, Y. Wang, T. Sanegira, S. Merckel, S. Mei, *J. Geophys. Res.* **117**, B01203 (2012).
14. J. Gasc *et al.*, *Phys. Earth Planet. Inter.* **189**, 121–133 (2011).
15. A. Ougier-Simonin, J. Fortin, A. Schubnel, Y. Guéguen, F. Bouyer, *Int. J. Eng. Sci.* **49**, 105–121 (2011).
16. B. Gutenberg, C. F. Richter, *Nature* **176**, 795–795 (1955).
17. C. H. Scholz, *Bull. Seismol. Soc. Am.* **58**, 399–415 (1968).
18. H. Kanamori, D. L. Anderson, T. H. Heaton, *Science* **279**, 839–842 (1998).
19. G. Di Toro *et al.*, *Nature* **471**, 494–498 (2011).
20. M. Antolik, D. Dreger, B. Romanowicz, *J. Geophys. Res.* **104**, 863–894 (1999).
21. G. A. Prieto, G. C. Beroza, S. A. Barett, G. A. López, M. Florez, *Tectonophysics* **570–571**, 42–56 (2012).
22. A. M. Boullier, Y. Guéguen, *Contrib. Mineral. Petrol.* **50**, 93–104 (1975).
23. T. Hiraga, T. Miyazaki, M. Tasaka, H. Yoshida, *Nature* **468**, 1091–1094 (2010).
24. F. X. Passelègue, A. Schubnel, S. Nielsen, H. S. Bhat, R. Madariaga, *Science* **340**, 1208–1211 (2013).
25. C. R. Bina, S. Stein, F. C. Marton, E. M. Van Ark, *Phys. Earth Planet. Inter.* **127**, 51–66 (2001).
26. T. Iidaka, D. Suetsugu, *Nature* **356**, 593–595 (1992).
27. H. Kawakatsu, S. Yoshioka, *Earth Planet. Sci. Lett.* **303**, 1–10 (2011).
28. D. A. Wiens, J. J. McGuire, P. J. Shore, *Nature* **364**, 790–793 (1993).
29. R. Myhill, *Geophys. J. Int.* **192**, 837–853 (2012).
30. J. A. Hudson, R. G. Pearce, R. M. Rogers, *J. Geophys. Res.* **94**, 765–774 (1989).

Energy Release of the 2013 M_W 8.3 Sea of Okhotsk Earthquake and Deep Slab Stress Heterogeneity

Lingling Ye,[1] Thorne Lay,[1]* Hiroo Kanamori,[2] Keith D. Koper[3]

Earth's deepest earthquakes occur in subducting oceanic lithosphere, where temperatures are lower than in ambient mantle. On 24 May 2013, a magnitude 8.3 earthquake ruptured a 180-kilometer-long fault within the subducting Pacific plate about 609 kilometers below the Sea of Okhotsk. Global seismic *P* wave recordings indicate a radiated seismic energy of ~1.5×10^{17} joules. A rupture velocity of ~4.0 to 4.5 kilometers/second is determined by back-projection of short-period *P* waves, and the fault width is constrained to give static stress drop estimates (~12 to 15 megapascals) compatible with theoretical radiation efficiency for crack models. A nearby aftershock had a stress drop one to two orders of magnitude higher, indicating large stress heterogeneity in the deep slab, and plausibly within the rupture process of the great event.

The occurrence of earthquakes in the depth range from 400 to 720 km (the mantle transition zone) has long been enigmatic, given the immense pressure exerted by the overlying rock mass on any fault surface. Seismic radiation from deep earthquakes indicates that they likely involve shear faulting basically indistinguishable from shallow earthquakes despite the extreme pressure conditions. Deep earthquakes only initiate in relatively low-temperature regions of subducted oceanic lithosphere. Very high deviatoric stresses may be present in the core of the subducted slab, and some mechanism must exist to offset the inhibiting effects of pressure to allow shear faulting to initiate (1). For the depth range from 50 to 400 km, it is generally believed that

release of water by mineral dehydration reactions or production of other fluid phases reduces the effective normal stress on surfaces and enables fluid-assisted frictional sliding. It is not clear whether such mechanisms can account for transition-zone earthquakes, the largest of which tend to occur below a 600-km depth. Much research has focused on processes such as abrupt phase transitions (2) that may be able to nucleate rupture under tremendous confining stress. Once deep fault slip initiates and becomes substantial, frictional heating can lead to melting of the fault surface, abetting runaway rupture expansion for large deep earthquakes (3).

On 24 May 2013 the largest deep earthquake yet recorded occurred near a depth of 609 km [05:44:49 UTC, 54.874°N, 153.281°E (4)] in the Pacific plate subducting along the Kuril-Kamchatka subduction zone (Fig. 1). The event locates under the Sea of Okhotsk. Globally recorded long-period seismic waves indicate that the overall earthquake process appears to involve shear faulting with a seismic moment of ~4.1×10^{21} N·m [moment magnitude (M_w) = 8.3] (4, 5). The event is slightly larger than the 637-km-deep Bolivia earthquake of 9 June 1994 that had a seismic moment of ~3×10^{21} N·m (M_w = 8.3) (6, 7).

Both great events have similar faulting geometries with very shallow-dipping normal fault mechanisms and only minor deviations from shear double-couple solutions. The 1994 Bolivia

[1]Department of Earth and Planetary Sciences, University of California Santa Cruz, Santa Cruz, CA 95064, USA. [2]Seismological Laboratory, California Institute of Technology, Pasadena, CA 91125, USA. [3]Department of Geology and Geophysics, University of Utah, Salt Lake City, UT 84112, USA.

*Corresponding author. E-mail: tlay@ucsc.edu

Fig. 1. Tectonic setting of the 2013 M_w 8.3 deep Sea of Okhotsk slab earthquake. (Inset) The plate configuration, with the Pacific plate underthrusting the North American/Sea of Okhotsk plate along the Kuril-Kamchatka subduction zone at a convergence velocity of ~8.0 cm/year. Dashed lines are depth contours for the subducted oceanic slab beneath the Sea of Okhotsk. The main map shows best-double couple faulting mechanisms from global centroid-moment tensor inversions for recent large earthquakes in the deep slab, with blue indicating events below 600 km depth and cyan indicating events around 500 km deep. Focal mechanisms are at the event epicenter unless offset with a tie line. Small circles are locations of aftershocks of the 24 May 2013 event with magnitudes from 4.1 to 4.4. The contoured plot indicates the slip distribution of the preferred rupture model for the mainshock, with the large red star being the hypocenter at a depth of 608.9 km. The arrows indicate the magnitude and the direction of slip of the upper side of the fault, with the fault dipping 10° toward the west. The peak slip is 9.9 m, and the colors indicate about 2.2-m slip contour increments.
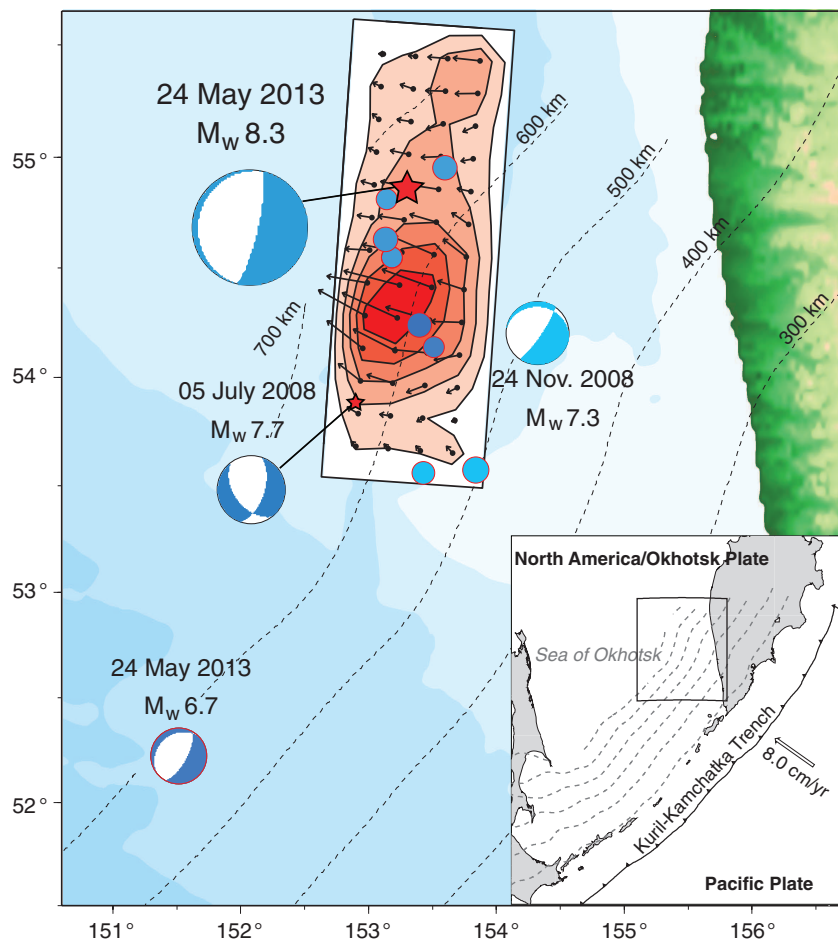
Fig. 2. Source spectra estimates for the 2013 M_w 8.3 Sea of Okhotsk mainshock and M_w 6.7 aftershock. The mainshock spectrum is estimated by two methods. The blue curves are estimates based on the spectrum of the source time function from finite-fault inversion for frequencies less than 0.05 Hz and from averaging many teleseismic P wave spectra with propagation and radiation pattern corrections from 0.05 to 3.0 Hz. Results are shown for different attenuation parameters of $t^* = 0.1$ to 0.5 s. The red curve is an estimate of the mainshock source spectrum from 284 spectral ratios of the mainshock and the aftershock (EGF) spectra at the same station for the frequency band 0.03 to 0.25 Hz. The extrapolated spectra to 3 Hz assume source spectrum decay exponents from -1.0 to -2.0. The green curve is the average source spectrum for the M_w 6.7 event based on the first method, using an assumed $t^* = 0.3$ s. **(Inset)** The dependence of estimates of E_R on the assumed value of t^* for the mainshock signals, given by averaging energy estimates from individual path-corrected P wave spectra.
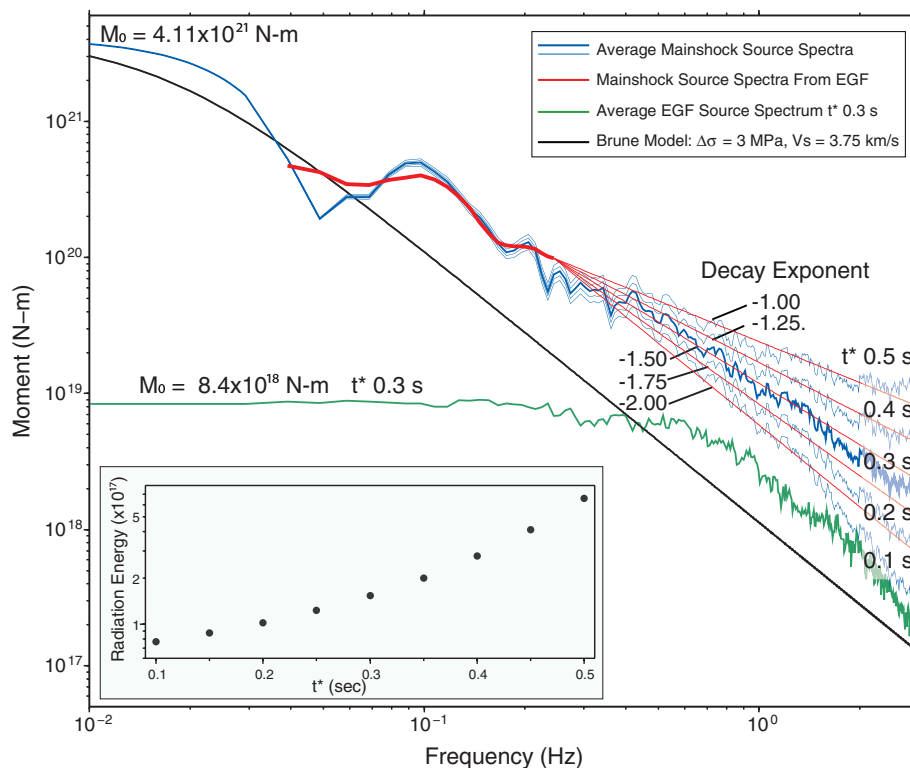
earthquake was interpreted as having a relatively slow rupture velocity, $V_r \sim 1$ to 2 km/s, with an ~40-s rupture duration and a spatially compact rupture zone with a scale of about 40 km by 60 km (6–11), leading to large stress drop estimates of around 110 to 150 MPa (7, 11).

In the first 4 days after the 2013 earthquake, nine aftershocks were detected, eight having small magnitudes of 4.1 to 4.4 at depths from 487 to 627 km, and an $M_w = 6.7$ event struck 9 hours after the mainshock [14:56:31, 52.222°N, 151.515°E, 623 km deep (4)] about 200 km to the southwest (Fig. 1). Six nearby aftershocks with depths of around 600 km define a north-south trend about 90 km long, preferentially extending southward from the mainshock hypocenter. The trend is generally compatible with rupture along either of the two nodal planes of the mainshock focal mechanism but slightly favors the shallow plane. Aftershock occurrence for large deep earthquakes is highly variable (12), and the large depth range for the 2013 aftershocks suggests that some are triggered away from the mainshock rupture zone. The 2013 event was preceded by nearby large earthquakes in 2008 ($M_w = 7.3$ and 7.7, Fig. 1), the larger of which was ~100 km along strike to the south.

Two of the most fundamental seismological properties of a large earthquake are the source spectrum and the radiated seismic energy. We analyzed extensive global seismic recordings of P waves for the 2013 event to estimate both. Source spectrum estimates obtained from two distinct approaches provide estimates of the radiated seismic energy (Fig. 2). The radiated energy estimates depend on attenuation corrections. The attenuation corrections are parameterized by t^*, the ratio of total P wave travel time to average attenuation quality factor, $Q(f)$, along each path as a function of frequency, f. The precise $Q(f)$ on each path is not known in detail and is expected to vary strongly because of upper mantle heterogeneity in attenuation structure beneath the seismic stations. For deep focus earthquakes, the t^* values are expected to be on average ~0.5 s at 0.1 Hz for teleseismic P waves (half of the t^* value for a shallow source) and about 0.25 to 0.5 s at 1.0 Hz, with t^* likely decreasing as frequency increases above 1.0 Hz. Lacking knowledge of specific path or even best average attenuation parameters, we show spectral estimates for a range of constant t^* values from 0.1 to 0.5 s, with a value of 0.3 s deemed to be a reasonable value. The uncertainty in t^* affects the high-frequency spectral levels, which are very important for radiated seismic energy estimates. We averaged the energy values obtained from 102 stations by integrating the energy spectrum from the P-wave ground-motion velocities (13–16) after correcting for faulting geometry and propagation effects. Use of $t^* = 0.3$ s for each station and frequencies up to 3 Hz gives radiated energy of $E_R = 1.5 \times 10^{17}$ J, with a range of reasonable estimates being given by results for $t^* = 0.2$ s ($E_R = 1.0 \times 10^{17}$ J) to 0.4 s ($E_R = 2.8 \times 10^{17}$ J).

For $t^* = 0.3$ s, the moment-scaled energy is $E_R/M_0 = 3.7 \times 10^{-5}$.

To confirm the source spectrum estimate, we used P-wave observations of the nearby M_w 6.7 aftershock at the same stations as for the mainshock to explicitly cancel out the unknown path effects. The large aftershock is remarkably short duration, with impulsive P wave motions that have average pulse widths of about 1.8 s. The average source spectrum for the aftershock found assuming $t^* = 0.3$ s for 22 stations has a very flat spectrum up to ~0.5 Hz (Fig. 2), indicating that this event can serve as an impulse response, or empirical Green's function (EGF), up to near that frequency. For $t^* = 0.3$ s, E_R is 2.36×10^{15} J for the EGF from log averaging of the 22 individual station energies, and E_R/M_0 is 2.8×10^{-4} using our finite-fault inversion estimates of the seismic moment $M_0 = 8.4 \times 10^{18}$ N·m.

We computed mainshock/EGF spectral ratios for 284 broadband P-wave observations (fig. S1), correcting for differences in radiation pattern, geometric spreading, and multiplying by the EGF M_0. The ratios are in close agreement with the averages of mainshock P spectra over the corresponding passband (Fig. 2). This ensures that uncertainties in t^* do not bias the average spectrum estimate in this passband.

Extrapolations of the spectral ratios from 0.25 to 3.0 Hz are made for various assumed mainshock spectral decay slopes with frequency ex-

ponents varying from –1 to –2. For reference, a shallow interplate earthquake source spectrum for a moment equal to that of the mainshock has a decay exponent of –2, a stress parameter of 3 MPa, and source velocity of 3.75 km/s. The deep earthquake spectral amplitudes are enriched in high frequency relative to the reference model, in part because of higher source velocity and in part because of higher stress drop. The precise spectral decay slope expected near 1 Hz is not known, because it depends on the detailed space-time history of slip on the fault, but values around –1.5 to –2 are consistent with assuming t^* values around 0.3 s. We conclude that $E_R \sim 1.5 \times 10^{17}$ J, with about a factor of 2 uncertainty. This is about three times as large as for the 1994 Bolivia event [$E_R \sim 5.2 \times 10^{16}$ J (3, 17)].

The spatial extent of the 2013 Sea of Okhotsk deep earthquake faulting is critical for estimating additional properties of the source, such as slip pattern and static stress drop. Back-projection of teleseismic short-period P waves was used to estimate V_r and the source rupture dimensions (Fig. 3). The data are from large continental seismic networks in Europe and North America that recorded coherent broadband waveforms (fig. S4). For both array geometries, the back-projections indicate asymmetric bilateral extent of short-period radiation extending 50 to 60 km to the north of the hypocenter and about 120 km to the south, along the trend of the deep after-

Fig. 3. Constraints on rupture velocity from P wave back-projection. Teleseismic P waves in the frequency band from 0.5 to 2.0 Hz from large networks of stations in North America (NA) and Europe (EU) were used to image the space-time history of coherent high-frequency seismic radiation from the 2013 M_w 8.3 Sea of Okhotsk earthquake. The time-integrated power stacked on a grid around the source are shown here relative to the mainshock epicenter (white stars). The darker blue colors indicate coherent energy release with an asymmetric spread of source radiation in the north-south direction being resolved by the images from both networks. movie S1 shows the time-varying images throughout the rupture process.
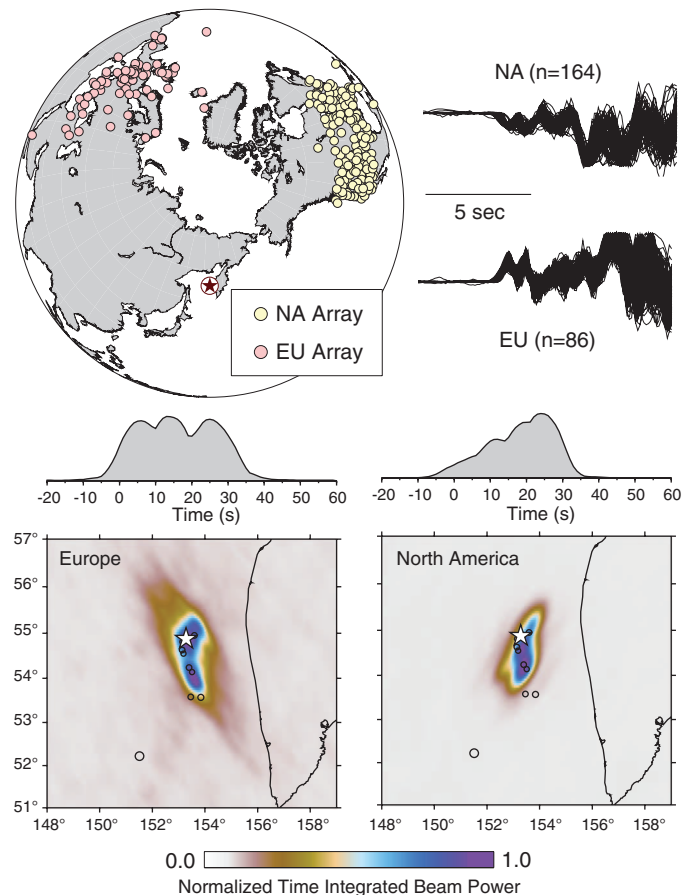
shocks, with a source time duration of about 30 s. Animations of the back-projections show the space time evolution of the short-period radiation (movie S1).

If we adopt the V_r estimate of 4.0 km/s obtained from the back-projections as a constraint on the finite-fault inversions, we find rupture models with average slip of 1.9 to 2.3 m and an average static stress drop of 4 to 5 MPa for rupture areas that have a radius of about 74 to 82 km (figs. S2 and S3) for the two fault plane choices. For these estimates, only subfaults with moment at least 15% of the peak subfault moment were retained to diminish sensitivity to poorly resolved low-slip areas of the model (*18*).

A problem with these solutions is that they can give large (>1) estimates of calculated radiation efficiency, η_R, which is the ratio of E_R to the available potential energy, ΔW_0:

$$\eta_R = E_R/\Delta W_0 = 2\mu E_R/(\Delta\sigma_s M_0)$$

where $\Delta\sigma_s$ is the static stress drop and μ is the rigidity.

Radiation efficiency has been calculated as a function of V_r for mode II, mode III, and energy-based (mode E) crack models (Fig. 4) (*19–23*). For higher V_r, there is less energy dissipation near the crack tip, so the radiation efficiency approaches 1 as V_r approaches the limiting speed (the Rayleigh velocity for mode II and the shear velocity for mode III and mode E). For the 2013 Sea of Okhotsk event, $V_r < 2.5$ km/s is required for the circularly expanding rupture models to have large enough calculated stress drop to lower the seismic efficiency to intersect the predictions of crack theory (Fig. 4). Such a low V_r cannot account for the faulting dimensions indicated by

the back-projections for the 2013 Sea of Okhotsk event. In order to obtain radiation efficiency consistent with the crack models, the width of the ruptures for high V_r must be constrained, essentially increasing the static stress drop by imposing rectangular rather than circular fault expansion.

For $V_r = 4.0$ km/s, $\Delta\sigma_s = 15$ MPa is needed to give $\eta_R = 0.6$ for a mode III rupture (Fig. 4). For a 180-km rupture length, imposing a fault width of 60 km yields an effective rupture area that gives the required stress drop. For $V_r = 5$ km/s, the fault width is increased to 68 km and gives $\Delta\sigma_s = 12$ MPa and $\eta_R = 0.75$ (Fig. 4). These models are now physically acceptable, and the slip distribution for the shallow-dipping plane for $V_r = 4$ km/s has average slip of 4.4 m (Fig. 1 and fig. S9a). Good fits to observed P waveforms are obtained (fig. S10). The slip distribution has asymmetric bilateral extent of 60 km north northeast and 120 km south southwest. Large slip is concentrated between 30 and 90 km south of the hypocenter, with the area of significant slip being 9675 km^2. We have some preference for the shallow-dipping plane, but very similar results are found for the steeply dipping plane (fig. S9b); the narrow rectangular faults give similar waveforms at most stations for the along-strike rupture.

Although there are limitations in the precision of the back-projection constraints and the theoretical crack-model efficiency is calculated for very simple models, the basic model with $V_r \sim 4.0$ km/s and $\Delta\sigma_s \sim 15$ MPa appears to be a valid representation of the overall source rupture. The V_r and rupture area are both about a factor of 4 larger than for the 1994 Bolivia event, and $\Delta\sigma_s$ is about an order of magnitude lower. The $\Delta\sigma_s \sim 15$ MPa estimate is comparable to val-

ues for shallow intraplate earthquakes (*13, 24, 25*), and the fault dimensions are similar to those for the shallow trench-slope intraplate normal faulting event in the Kuril Islands of 13 January 2007 ($M_w = 8.1$) (*26*). The fault geometry is compatible with rerupture of such an outer rise normal fault surface within the plate, rotated by the dip of the deep slab. However, the $M_w = 6.7$ aftershock has an unusually short rupture duration and finite-fault inversions for variable assumed rupture velocities for that event give $\Delta\sigma_s$ estimates in the range 157 to 5856 MPa (fig. S12). Independent constraints on the aftershock fault area or rupture velocity are not available, but there is no question that it has a localized stress drop greatly exceeding the average stress drop for the 8.3 mainshock and substantially lower radiation efficiency suggestive of a more dissipative source process. It is plausible that within the mainshock rupture zone there were corresponding very high stress drop slip patches that cannot be resolved. The envelope of teleseismic P-wave ground accelerations for the mainshock follows the source-time function shape (fig. S13), so a very heterogeneous stress distribution on the fault does appear likely (*27–29*), and the average parameters do not represent the total degree of slip and stress heterogeneity.

The 2013 mainshock rupture extends along the slab strike, with slip likely confined to the low temperature core of the slab. The subducted plate is older and colder than the slab where the 1994 Bolivia earthquake occurred, and this difference in thermal state may have fundamentally affected how rupture expanded for the two events (*30*). The Sea of Okhotsk event is similar to a shallow intraplate earthquake, with a large aspect ratio fault area defined by the brittle core of the slab. For the Bolivia event, the brittle core volume is smaller, and surrounding ductile or plastic material with a finite strength may dominate. Faulting for the Bolivia event involved a rupture with a very dissipative source process that deposited a large amount of energy into the rupture zone, likely leading to melting. This behavior may be akin to that of a shear band. The Sea of Okhotsk mainshock rupture appears to have been less dissipative, and little or no melting may have occurred, although seismology cannot directly constrain the amount of melting.

The stress drops found for the 2013 mainshock and large aftershock suggest preexisting zones with strong and weak regions, likely inherited from shallow faulting of the slab. The warm plate in Bolivia may have more strong, less-brittle patches than weak-brittle patches, whereas the cold plate in the Sea of Okhotsk has more weak-brittle patches than strong, less-brittle patches. Strong patches may be distributed only sparsely in the Sea of Okhotsk slab, with one rupturing in the aftershock, and may act to stop rupture propagation on weak patches. The difference in the distribution of strong, less-brittle and weak-brittle patches caused by the difference in the thermal state is likely responsible

Fig. 4. Model constraints from consideration of radiation efficiency for crack models with varying rupture speed. Reference curves for mode II and mode III cracks and an energy-based model (mode E) have η_R values that approach 1 as the rupture speeds approach their limiting velocities (~5.1 km/s for mode II, ~5.5 km/s for mode III and mode E at a depth of 610 km) (*16, 23*). The blue circles indicate calculated radiation efficiencies for rupture models (fig. S2) with varying V_r and fault dimensions scaling proportional to V_r. These

models are only compatible with the crack theory for $V_r \sim 1.5$ to 2.0 km/s, but this is inconsistent with the rupture extent indicated by back-projection in Fig. 3, which favors V_r of 4.0 to 5.0 km/s. By constraining the width of the slip models, we find high-V_r models consistent with the theoretical radiation efficiency, with preferred models giving the red stars. The solution shown in Fig. 1 is the 15-MPa stress drop model for $V_r = 4.0$ km/s. The pink bars indicate variation in estimates for different thresholds (0.1 to 0.2, with stars for 0.15) used to remove poorly resolved low slip regions of the fault models.
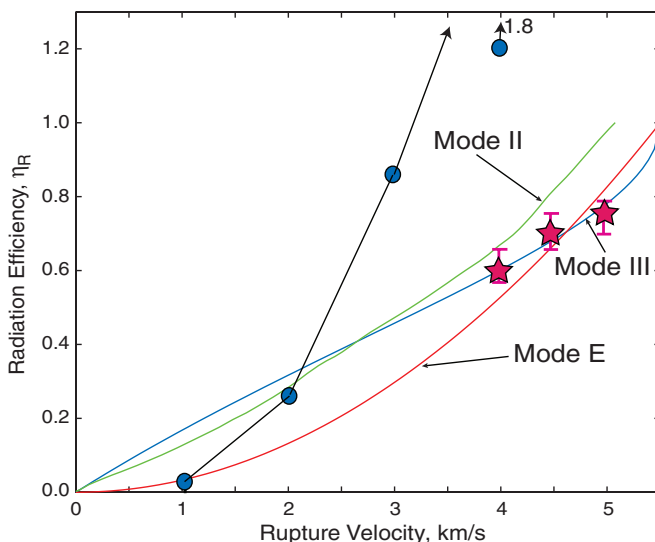
for the drastically different source characteristics of the Bolivian and the Sea of Okhotsk events.

References and Notes

1. H. W. Green II, H. Houston, *Annu. Rev. Earth Planet. Sci.* **23**, 169–213 (1995).
2. H. W. Green II, P. C. Burnley, *Nature* **341**, 733–737 (1989).
3. H. Kanamori, D. L. Anderson, T. H. Heaton, *Science* **279**, 839–842 (1998).
4. U.S. Geological Survey, http://earthquake.usgs.gov/earthquakes/eventpage/usb000h4jh#summary.
5. Global Centroid Moment Tensor Project, www.globalcmt.org/CMTsearch.html.
6. P. G. Silver *et al.*, *Science* **268**, 69–73 (1995).
7. M. Kikuchi, H. Kanamori, *Geophys. Res. Lett.* **21**, 2341–2344 (1994).
8. S. L. Beck, P. Silver, T. C. Wallace, D. James, *Geophys. Res. Lett.* **22**, 2257–2260 (1995).
9. P. F. Ihmlé, *J. Geophys. Res.* **103**, 17,919 (1998).
10. W.-P. Chen, *Geophys. Res. Lett.* **22**, 2261–2264 (1995).
11. M. Antolik, D. Dreger, B. Romanowicz, *Geophys. Res. Lett.* **23**, 1589–1592 (1996).
12. D. A. Wiens, J. J. McGuire, *Geophys. Res. Lett.* **22**, 2245–2248 (1995).
13. A. Venkataraman, H. Kanamori, *J. Geophys. Res.* **109**, B05302 (2004).
14. L. Rivera, H. Kanamori, *Geophys. J. Int.* **162**, 148–155 (2005).
15. H. Kanamori, L. Rivera, *AGU Geophys. Monogr.* **170**, 3–13 (2006).
16. A. V. Newman, E. A. Okal, *J. Geophys. Res.* **103**, 26885 (1998).
17. N. W. Winslow, L. J. Ruff, *Phys. Earth Planet. Inter.* **115**, 181–190 (1999).
18. H. Noda, N. Lapusta, H. Kanamori, *Geophys. J. Int.* **193**, 1691–1712 (2013).
19. L. B. Freund, *J. Elast.* **2**, 341–349 (1972).
20. A. F. Fossum, L. B. Freund, *J. Geophys. Res.* **80**, 3343–3347 (1975).
21. B. V. Kostrov, *J. Appl. Math. Mech. Engl. Transl.* **30**, 1241–1248 (1966).
22. N. F. Mott, *Engineering* **165**, 16 (1948).
23. H. Kanamori, E. Brodsky, *Rep. Prog. Phys.* **67**, 1429–1496 (2004).
24. B. P. Allmann, P. M. Shearer, *J. Geophys. Res.* **114**, B01310 (2009).
25. J. A. Convers, A. V. Newman, *J. Geophys. Res.* **116**, B08304 (2011).
26. T. Lay *et al.*, *J. Geophys. Res.* **114**, B11308 (2009).
27. H. Houston, H. M. Benz, J. E. Vidale, *J. Geophys. Res.* **103**, 29895 (1998).
28. W.-Y. Chung, H. Kanamori, *Phys. Earth Planet. Inter.* **23**, 134–159 (1980).
29. L.-R. Wu, W.-P. Chen, *Bull. Seismol. Soc. Am.* **91**, 102–111 (2001).
30. R. Tibi, G. Bock, D. A. Wiens, *J. Geophys. Res.* **108**, 2091 (2003).

Nonlegumes Respond to Rhizobial Nod Factors by Suppressing the Innate Immune Response

Yan Liang,[1] Yangrong Cao,[1] Kiwamu Tanaka,[1] Sandra Thibivilliers,[1]* Jinrong Wan,[2] Jeongmin Choi,[1] Chang ho Kang,[3] Jing Qiu,[4] Gary Stacey[1]†

Virtually since the discovery of nitrogen-fixing *Rhizobium*-legume symbioses, researchers have dreamed of transferring this capability into nonlegume crop species (for example, corn). In general, nonlegumes were assumed to lack the ability to respond to the rhizobial lipo-chitin Nod factors, which are the essential signal molecules that trigger legume nodulation. However, our data indicate that *Arabidopsis thaliana* plants, as well as other nonlegumes, recognize the rhizobial Nod factor via a mechanism that results in strong suppression of microbe-associated molecular pattern (MAMP)–triggered immunity. The mechanism of action leads to reduced levels of pattern-recognition receptors on the plasma membrane involved in MAMP recognition.

A general theory for the development of commensal and mutualistic symbioses is that they evolved from pathogenic relationships (*1*). Although the *Rhizobium*-legume symbiosis is beneficial and benign, the plant initially responds with a pathogen defense response that is quickly suppressed (*2*, *3*). The lipo-chitin nodulation factors (known as Nod factors) are substituted acylate chitin oligomers of three to five *N*-acetylglucosamine residues and are the key signaling molecules for the establishment of *Rhizobium*-legume symbioses. These factors induce plant responses that lead to the development of the nodule, which becomes the intracellular home of the invading symbiont (*4*, *5*). Nod factors function at nanomolar levels (*6*, *7*), but on only specific, compatible legume hosts. Extension of nitrogen-fixing symbioses beyond these already compatible legume hosts could help reduce dependence on applied fertilizers (*8*).

Plant innate immunity can be triggered by the recognition of microbe-associated molecular patterns (MAMPs) (*9*). The best-studied MAMP is bacterial flagellin (flg22, a conserved 22–amino acid peptide from flagellin), which is recognized by the FLAGELLIN-SENSING 2 (FLS2) receptor located on the plasma membrane (*10*). Perception of flg22 activates a signaling cascade of defense responses, including calcium influx (*11*), reactive oxygen species (ROS) production (*12*), activation of mitogen-activated protein (MAP) kinases (*13*), gene expression (*14*), callose deposition (*15*), and bacterial growth restriction (*10*).

Together, these responses are called MAMP-triggered immunity.

To study the intersection between symbiosis and pathogenesis, we added both flg22 and purified Nod factor from *Bradyrhizobium japonicum*, the soybean symbiont, to soybean leaves (see supplementary materials and methods). The flg22-triggered ROS production was reduced 25% in the presence of Nod factor (Fig. 1A). Chitin is also a strong MAMP but only when the oligomers have more than six *N*-acetylglucosamine residues. Nod factor is composed of shorter oligomers (three to five residues). We tested the chitin oligomers containing one to eight residues for their ability to suppress flg22-triggered ROS production. Chitotetraose (C4) and chitopentaose (C5) reduced flg22-triggered ROS production, but not as efficiently as Nod factor (fig. S1). Chitin oligomers C6 through C8 did not affect flg22-triggered ROS production (fig. S1). These results are similar to some symbiotic responses in which simple chitooligomers can suffice but only at higher concentration than the Nod factor (*16*, *17*). Treatment with Nod factor or chitotetraose alone did not induce ROS production (Fig. 1A). Pretreatment of plants with Nod factor or chitotetraose enhanced the suppressive effect of flg22-triggered ROS production (Fig. 1B). For example, flg22-induced ROS production was reduced 60% with 30 min of chitotetraose pretreatment (Fig. 1B).

The suppressive effects of Nod factor or chitotetraose addition were also seen when chitooctaose, a potent MAMP, was used to induce ROS production (fig. S2). During nodulation, application of Nod factors at picomolar to nanomolar concentrations elicits a variety of symbiotic responses (for instance, root hair deformation). The lowest concentration of Nod factor required to reduce flg22-triggered ROS production was 1 nM (Fig. 1C). One of the downstream signals after flg22 treatment in *Arabidopsis* is MAP kinase phosphorylation, which can be detected immuno-

[1]Divisions of Plant Science and Biochemistry, National Center for Soybean Biotechnology, Christopher S. Bond Life Sciences Center, University of Missouri, Columbia, MO 65211, USA. [2]Division of Plant Science, 46 Agriculture Building, University of Missouri, Columbia, MO 65211, USA. [3]Plant Molecular Biology and Biotechnology Research Center, Gyeongsang National University, Building 6-421, Jinjudaero 501, JinJu, Gyeongsangnam-do, 660-701, South Korea. [4]Department of Statistics, 134I Middlebush Hall, University of Missouri, Columbia, MO 65211, USA.

*Present address: Department of Microbiology and Plant Biology, University of Oklahoma, Norman, OK 73019, USA.
†Corresponding author. E-mail: staceyg@missouri.edu

Supplementary Materials for

Energy Release of the 2013 M_w 8.3 Sea of Okhotsk Earthquake and Deep Slab Stress Heterogeneity

Lingling Ye, Thorne Lay,* Hiroo Kanamori, Keith D. Koper

*Corresponding author. E-mail: tlay@ucsc.edu

This PDF file includes:

Other Supplementary Material for this manuscript includes the following:
available at www.sciencemag.org/content/341/6152/1380/suppl/DC1

Materials and Methods

1. Radiated Energy Estimation.

Teleseismic broadband P wave observations were analyzed for hundreds of recordings from stations of the Federation of Digital Seismic Networks (FDSN), accessed through the Incorporated Research Institutions for Seismology (IRIS) Data Management Center (DMC). High-quality signals were retained for the M_w 8.3 mainshock and M_w 6.7 aftershock for stations with computed P-wave radiation pattern coefficients higher than 0.5. Data were corrected for radiation pattern, instrument response, geometric spreading and attenuation parameterized with varying values of t^*. The low frequency portion of the average spectrum, below 0.05 Hz, is obtained from the source spectrum of the moment rate function determined by finite-fault inversion of teleseismic P waves and the long-period estimate of seismic moment, $M_0 = 4.1 \times 10^{21}$ Nm. The moment rate function characterizes the time history of the seismic radiation from the fault and is one of the most robust source attributes that can be determined using seismic waves. The higher frequency part of the source spectrum is obtained from averaging the corrected broadband P wave spectra for many stations. Subsets of 102 observations for the mainshock and 22 for the aftershock with good azimuthal distribution were used for computing individual estimates of seismic energy, and the estimates were averaged logarithmically to give the average radiated energy estimates and the average source spectra in Fig. 2.

284 pairs of recordings for the mainshock and aftershock with both signals having radiation pattern coefficients higher than 0.2 were used to compute the spectral ratio average in the passband 0.03-0.25 Hz. Examples of spectra are shown in Fig. S1. The individual spectral ratios were binned in 30° azimuthal windows and then averaged logarithmically to compute the mean value, scaled by the seismic moment of the aftershock, shown in Fig. 2.

2. Finite-fault model inversions.

We use a multi-time-window linear least-squares kinematic inversion procedure (*S1, S2*). Our initial finite-fault models (Fig. S2, S3) are parameterized with 17 nodes (central positions of subfaults) along strike and 17 nodes along dip with spacing proportional to imposed rupture velocity (3.75 km for 1 km/s, 7.5 km for 2 km/s, 11.25 km for 3 km/s, and 15 km for 4 km/s). We consider both nodal planes of the USGS W-phase point source moment tensor solution (best-double couple). The shallow-dipping plane has strike 184°, dip 10° and the steeply dipping plane has strike 12°, dip 81°. Each subfault source time function is parameterized with 4 2-s rise time symmetric triangles, allowing subfault rupture durations of up to 10 s. Rake is allowed to vary for each subevent of each subfault by allowing two rake values ±45° from the average given by the W-phase solution, with a non-negative moment constraint (*S3*). The hypocenter is 609 km deep. We apply Laplacian regularization, which constrains the second order gradient for each parameter to be zero.

75 teleseismic P wave records are used in the inversion, from global FDSN broadband seismic stations accessed through the IRIS-DMC. The data were selected from hundreds of available FDSN seismograms to have good azimuthal coverage (Figs. S9, S10) and high signal-to-noise ratios, for epicentral distances from 30° to 90°. The instrument responses are removed from the raw data to recover ground displacement records. A causal band-pass filter with corner frequencies at 0.003-0.9 Hz was applied to the data. The teleseismic Green's functions are generated with a reflectivity method that accounts for interactions in 1-D layered structures on both the source and receiver sides (*S2*). The PREM velocity structure is used in the modeling. A 60 s long time window of data with 10 s leader before the initial motion was used.

In finite-fault inversions, we usually start with a large enough fault plane to accommodate the slip zone well within it, with very low seismic moment on outer fringes of the fault model. Thus, it is necessary to trim the final slip distribution for estimating the effective rupture area. Trimming is done here by removing subfaults with a moment smaller than ξ times the moment of the subfault with the largest moment; we call ξ the trimming threshold. The purpose of trimming is twofold. First, it is to remove those subfaults with small amount of slip that can be regarded as noise in the inversion. For this purpose, a trimming threshold of ~10% is commonly used. Second, for purposes of estimating the strain energy, the stress drop to be used is $\Delta\sigma_E = \dfrac{\int_{\Sigma} \Delta\sigma_1 \Delta u_1 dS}{\int_{\Sigma} \Delta u_1 dS}$ which is the spatial average of stress drop weighted by slip. Unfortunately, it is difficult in practice to determine the slip distribution in sufficient detail to estimate its spatial distribution. Numerical models[18] have shown that $\Delta\sigma_E$ is always larger than the simple spatial average of the stress drop $\Delta\sigma$. Numerical calculations of $\Delta\sigma_E$ for many heterogeneous stress distributions indicate that a trimming threshold of from 0.15 to 0.3 can be used as a reasonable ratio for the purpose of estimating $\Delta\sigma_E$. We use 0.15 as the trimming parameter for all of our finite-fault models for the mainshock and aftershock. This value is slightly larger than commonly used in assessment of slip models, but it is larger not only to remove the insignificant subfaults but also to account for the effect of slip heterogeneity. Use of somewhat lower or higher trimming thresholds has negligible effects on our conclusions.

Very similar fits to global P waveforms were found for each case, despite large differences in spatial extent (Fig. S2). Slightly better fits are found using the horizontal plane, but the preference is subtle. With many-parameter space-time rupture models there is very little resolution of source finiteness for this event, as we also find to be true for the 1994 Bolivia event. Average slip values vary by a factor of 15 and static stress drop estimates by a factor of 50 for these models, so it is necessary to impose independent a priori constraints on *Vr* or fault dimensions to better constrain the source model.

The key equations for our radiation efficiency analysis are for the static stress drop for a buried rectangular fault:

3

$$\Delta\sigma_s = 16M_0 / (3\pi S_e W) \tag{1}$$

where S_e is the effective rupture area that gives a corresponding estimate $\Delta\sigma_E$ that we equate to the stress drop $\Delta\sigma_s$ and W is the fault width, and the radiation efficiency

$$\eta_R = E_R / \Delta W_0 = 2\mu E_R / (\Delta\sigma_s M_0) \tag{2}$$

From Fig. 4, for a given rupture velocity, we can infer a radiation efficiency value. With the measured radiated energy and seismic moment, and a rigidity appropriate for the source depth ($\mu = 121 \times 10^3$ MPa), we then know what value of stress drop will be compatible with the crack theory. For $Vr = 4$ km/s, $\eta_R = 0.6$ for the deep mainshock. This requires $\Delta\sigma_s = 15$ MPa for the Mode III crack model. Given the fault length required from P wave back-projections, we can then vary the fault width, W, for finite-fault inversions to give an inverted rupture area (for a specified trimming threshold) that yields the required stress drop. This leads to $W = 60$ km for the $Vr = 4$ km/s case. The effective rupture area in that case is 9675 km^2, using a trimming parameter of 0.15. For a fixed fault width, the stress drop estimate varies inversely with the effective source area by (1), or for a fixed stress drop, the width varies inversely with the effective source area. As the stress drop increases the radiated efficiency decreases for a fixed fault width. The degree to which one wants to match the crack theory ideal constrains the precision of the stress drop estimate desired and the corresponding constraint on the rupture model spatial extent.

Final models, constrained by the results of back-projections for apparent fault length and rupture velocity and by the radiation efficiency condition, involve rectangular fault models with asymmetric bilateral grids around the hypocenter. The models with $Vr = 4.0$ km/s in Fig. S9 have 4 grid points along dip and 13 along strike with 15 km spacing. The along-strike spacing for $Vr = 4.5$ and 5.0 km/s scales proportionally (16.9 km, 18.7 km, respectively), with the number of grid points along dip being kept the same, but along strike the number of grid points reduces to 12 and 11, respectively, to bound the total fault length. Other parameters and the data set are all the same as in the initial, unconstrained models. The data are well fit by these models (Fig. S10).

3. **Back-Projection of Teleseismic P waves**

Teleseismic P waves from four geographic groupings of broadband seismometers in North America (NA) (Fig. S4a,b), Europe (EU) (Fig. S4c,d), Alaska (Fig. S5), and Australia/Southeast Asia, as well as short-period Hi-net borehole stations in Japan (JA) (Fig. S6) were back-projected to the source region (*S4*) in order to image the short-period rupture properties of the 24 May 2013 Sea of Okhotsk earthquake and its aftershocks. Seismograms were selected from each region based on uniformity of spatial sampling and similarity of the first 10 s of the unfiltered P wavetrains as defined by the average cross-correlation coefficient (*cc*) determined from a multi-channel cross correlation algorithm (*S5*). This resulted in 74 traces with *cc* > 0.7 (AK), 67 traces with *cc* > 0.5 (AU), 86 traces with *cc* > 0.7 (EU), 409 traces with *cc* > 0.75 (JA), and 164 traces with *cc* > 0.65

(NA). For AU and NA the minimum similarity threshold was decreased slightly to increase the aperture of the array, which in turn increased the slowness resolution. For JA, only traces at distances greater than 15° from the nominal epicenter were selected in order to reduce the influence of waveform complexities created by interaction with the 660-km discontinuity.

For the mainshock back-projections the U. S. Geological Survey National Earthquake Information Center hypocenter of 54.874°N 153.281°E, h=608.9 km, 05:44:49 (UTC) was used as a reference point for aligning the waveforms. The source area was gridded in increments of 0.1° in latitude from 51° to 57° and in longitude from 148° to 159° and depth was held constant at the hypocentral value. Imaging time was sampled in 1 s intervals starting 20 s before the USGS origin time and continuing for 80 s. Power was calculated from a 10-s long, tapered window that slides along beams created with fourth-root stacking. Traces were bandpass filtered between 0.5 and 2 s prior to being stacked (for the results in Fig. 3), and a 10 s long smoothing filter was applied in post-processing to reduce artifacts. The AK135 reference Earth model was used to calculate travel times. The two arrays show source durations of about 30 s, with beam power extending in a ribbon-like geometry about 40-50 km to NNE and about 120-130 km to the SSE. The dimensions are consistent with an average rupture velocity of 4 to 5 km/s, although three or four short, subevent-like bursts of energy occur during the rupture and we cannot rule out lateral and temporal variations in the rupture velocity. Animations of the time-varying sequences for the NA and EU back-projections are presented in Movie M1.

The spatial resolution of the mainshock radiation for the AK and JA arrays is poorer than that for the EU and NA arrays, however, the AK and JA arrays are aligned more closely to the mainshock rupture direction and have sensitivity to the along-strike source finiteness. We illustrate this with vespagrams of the AK (Fig. S5) and JA (Fig. S6) data. In each case the aligned traces are filtered between 0.5-2.0 s and beams are created for relative slownesses between -0.4 and 0.4 s/deg (in increments of 0.01 s/deg) using 3rd order phase-weighting stacking (*S6*), a technique that amplifies coherent energy yet causes less waveform distortion than Nth root stacking. Power is calculated in a relative, logarithmic sense from envelopes of the stacks. Both arrays show source durations of approximately 30 s, consistent with the back-projection results, but also show a shift in differential slowness as the rupture progresses. Importantly, the AK vespagram shows a drift towards negative relative slowness, indicating steeper rays and thus longer source-receiver distances, while the JA vespagram shows a drift toward positive relative slowness, indicating shallower rays and thus shorter source receiver distances as the rupture progresses. Both vespagrams are thus consistent with southward directivity of the rupture.

We confirmed the mainshock finiteness observed for the NA and EU arrays by back-projecting data from two aftershocks with very simple sources: the M_w 6.7 event that occurred at 14:56:31 (UTC) on 24 May 2013 (52.222°N, 151.515°E, depth 623.0 km), and the m_b 4.4 event that occurred at 08:58:39 (UTC) on 28 May 2013 (54.241°N, 153.395°E, depth of 627.1 km). Results are presented in Fig. S7. The NA and EU array configurations used for the three events are very similar, though not exactly the same

because of lower quality or missing data for the aftershocks. In fact, not enough high-quality data were available to perform the EU back-projection for the smaller aftershock. Nevertheless, the simplicity of the three aftershock back-projections that were successful confirm that the finiteness observed in the mainshock back-projections is related to actual source complexity and is not created by any smearing artifact inherent to back-projection or any sort of wave propagation effect.

We further examined the stability of the EU and NA results by performing five additional back-projections in a series of narrow passbands centered at 0.5 s, 1 s, 2 s, 4 s, and 8 s. The gridding was the same as described above however the time averaging was scaled according the dominant period, with beam window lengths of 1.5 s, 3 s, 6 s, 12 s, and 24 s, respectively, and post-processing smoothing filter lengths of 4 s, 6 s, 14 s, 28 s, and 50 s. Results are presented in Fig. S8 and show relatively little spatial drift compared to back-projection images for recent megathrust earthquakes, implying that the short-period and long-period energy radiated by the mainshock were not in resolvably different spatial locations for this elongate rupture.

Synthetics were computed for the model in Fig. 1 for the same stations in Europe and North America used in the back-projections, and processed in the same manner. Resulting images for back-projection of the synthetics in various passbands for rectangular models with $Vr = 4.0$, 4.5 and 5.0 km/s are very consistent with the observations overall (Fig. S11). In detail, the data images appear to sense the rupture front rather than the peak-slip areas, as expected for seismic radiation from a dynamic rupture. The kinematic fault models do not accurately account for high frequency radiation at the crack tip. These results are very stable compared to back-projections for shallow events because there is no interference from surface reflections. We do not include surface reflections in the imaging given uncertainty in the slab structure and strong attenuation of the depth phases.
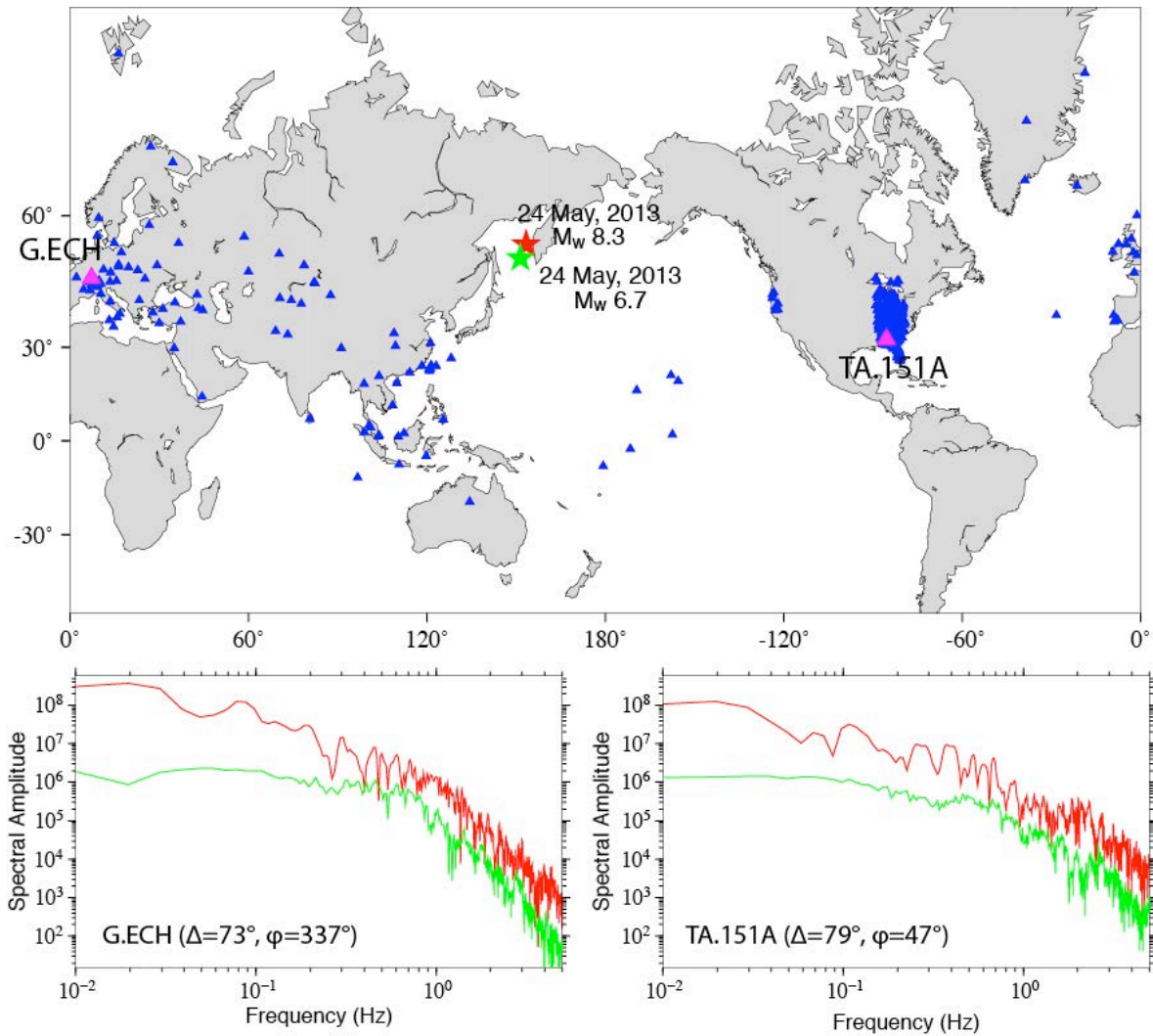
Fig. S1. Distribution of seismic stations used for spectral ratio analysis. The map shows the locations of 284 global broadband seismic network stations for which teleseismic P wave spectra were analyzed for the 24 May 2013 mainshock (M_w 8.3) (red star) and aftershock (M_w 6.7) (green star). Only stations with P wave radiation pattern coefficients larger than 0.2 for both events were used in the spectral ratio procedure. Example spectra from the stations with pink triangles on the map are shown below for the mainshock (red) and aftershock (green). Each station's epicentral distance (Δ) and azimuth (ϕ) are indicated. The spectra are corrected for relative radiation pattern and geometric spreading, but not for instrument response, which is common to the two events. The aftershock spectrum begins to drop off with frequency at around 0.5-0.6 Hz, which limits the range for which it serves as an empirical Green's function event. Spectral ratios in the passband 0.03-0.25 Hz are stacked and multiplied by the aftershock moment to obtain the mainshock source spectrum estimate in red in Fig. 2.
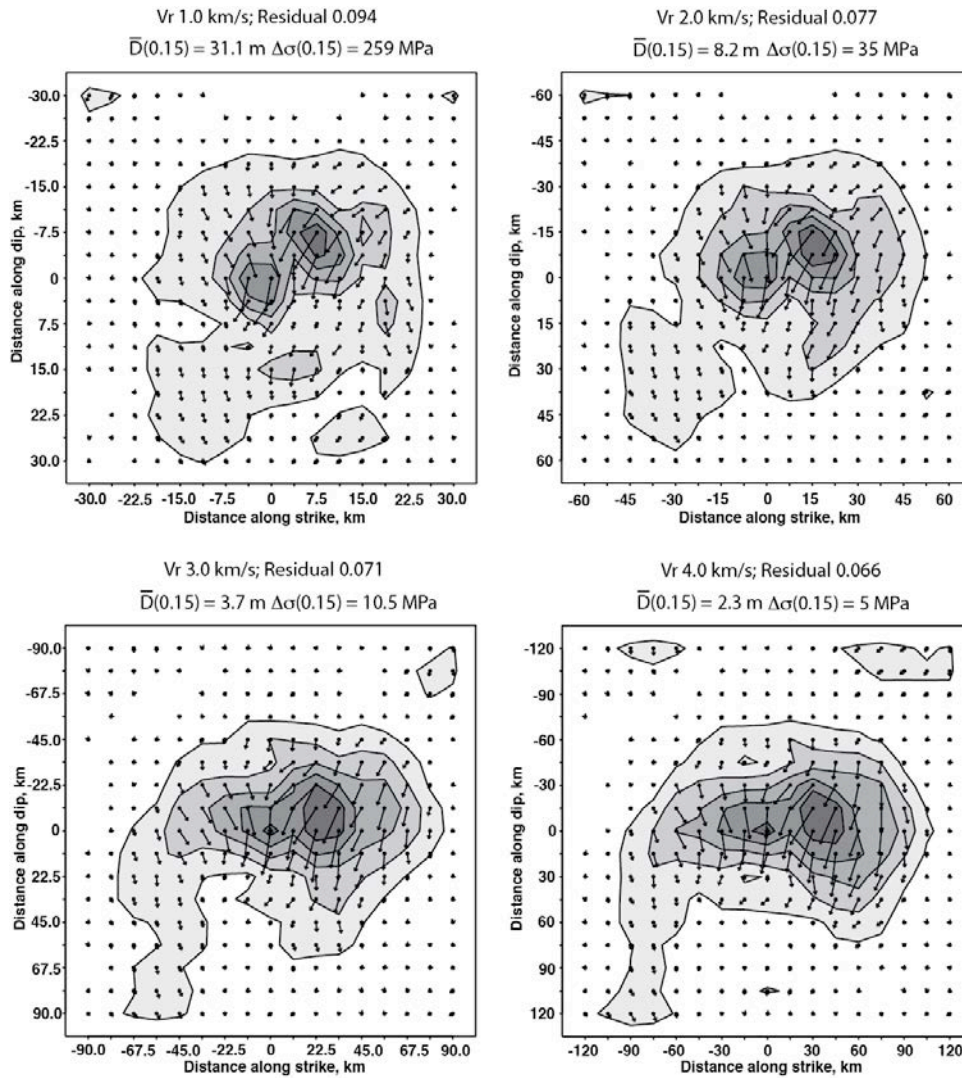
Fig. S2. Mainshock finite-fault models for varying rupture velocity for the shallow dipping plane. Slip distributions for four models with different constant rupture velocity with grid spacing scaling proportional to grid velocity. The strike is 184° and dip is 10° for all cases. Large model grids are used, with the hypocenter located at the center of each grid. For small Vr the rupture is relatively circular, but as it increases the model tends to elongate in the positive strike direction (toward the south). There is only about 3% greater reduction of the waveform mismatch for the much larger model for $Vr = 4.0$ km/s than for the very concentrated rupture for $Vr = 1.0$ km/s. For each model, the average displacement is computed for only those subfault sources with a seismic moment at least 15% as large as the largest sub-fault seismic moment and these values are given as D(0.15). Using the corresponding area of the remaining subfaults, a static stress drop is calculated using a circular rupture with radius matching the area of significant slip. There is about a factor of 50 range in stress drop estimate.
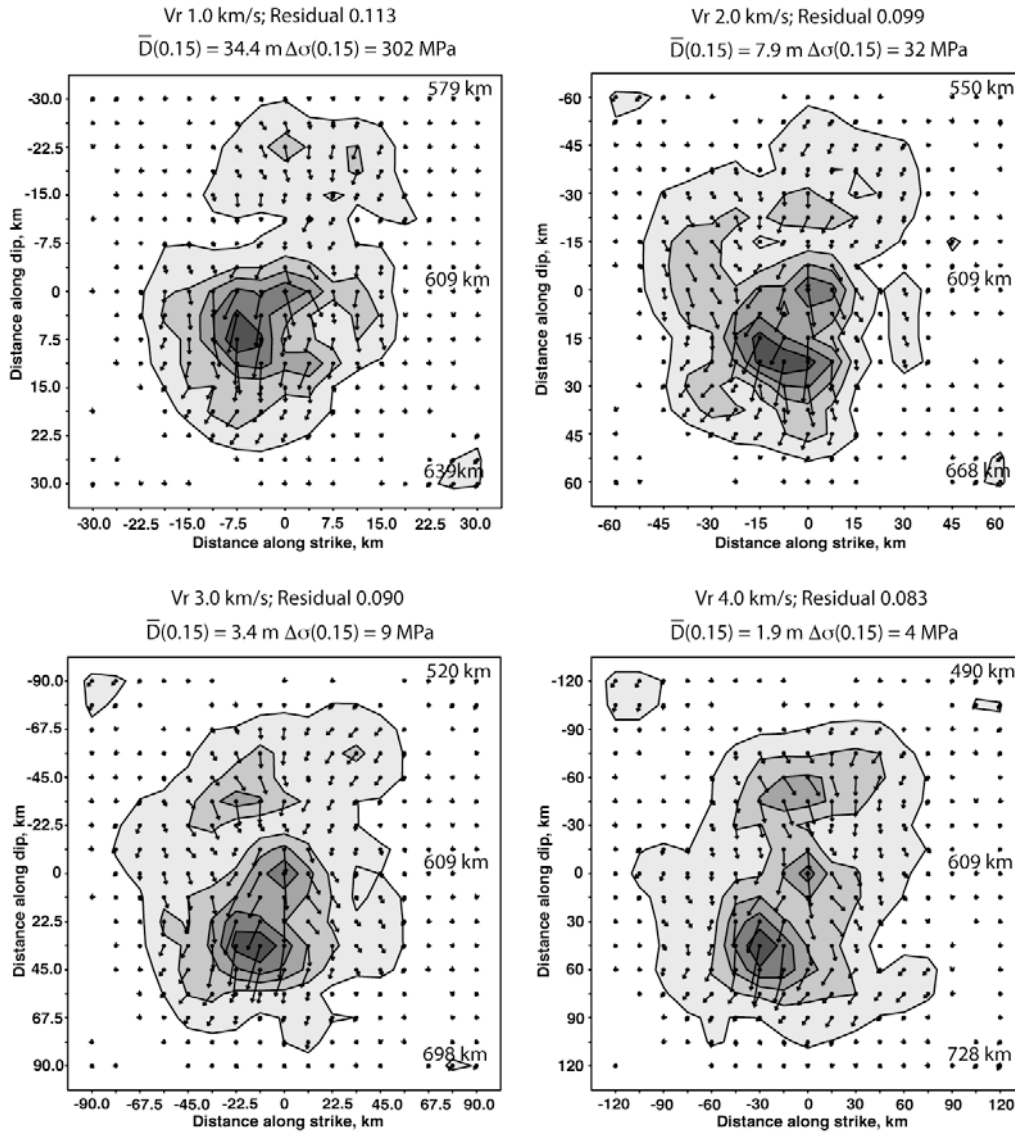
Fig. S3. Mainshock finite-fault models for varying rupture velocity for the steeply dipping plane. Slip distributions for four models with different constant rupture velocity with grid spacing scaling proportional to grid velocity. The strike is 12° and dip is 81° for all cases. Large model grids are used, with the hypocenter located at the center of each grid. For small *Vr* the rupture is relatively circular, but as it increases the model tends to elongate in the negative strike direction (toward the south). There is only about 3% greater reduction of the waveform mismatch for the much larger model for *Vr* = 4.0 km/s than for the very concentrated rupture for *Vr* = 1.0 km/s. For each model, the average displacement is computed for only those subfault sources with a seismic moment at least 15% as large as the largest sub-fault seismic moment and these values are given as D(0.15). Using the corresponding area of the remaining subfaults, a static stress drop is calculated using a circular rupture with radius matching the area of significant slip. There is about a factor of 76 range in stress drop estimate.
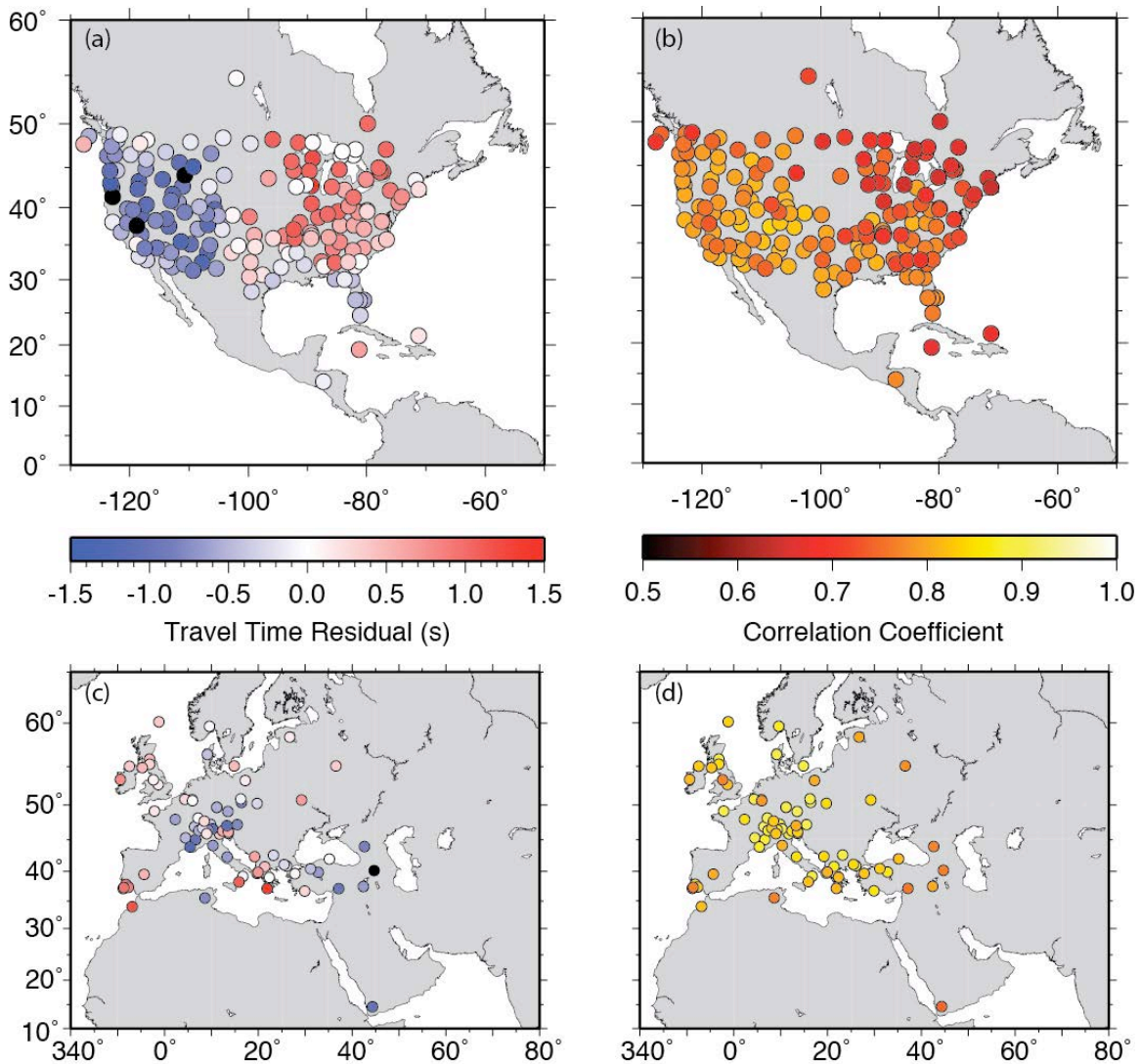
9

Fig. S4. Seismic station networks used for P wave back-projections. Maps of the broadband seismic station distributions in North America (a, b) and Europe (c, d) from which teleseismic P waves are obtained and back-projections to the source region performed. The station travel time residuals used to align the P waves, as determined by cross-correlation analysis are shown in (a) and (c), and the corresponding aligned trace correlation coefficients are shown in (b) and (d). The broadband traces were used for the alignment and then narrow-band filters were applied for back-projections of different passband signals. Fig. 3 shows the back-projection results for the 0.5-2.0 Hz passband data for the two networks.
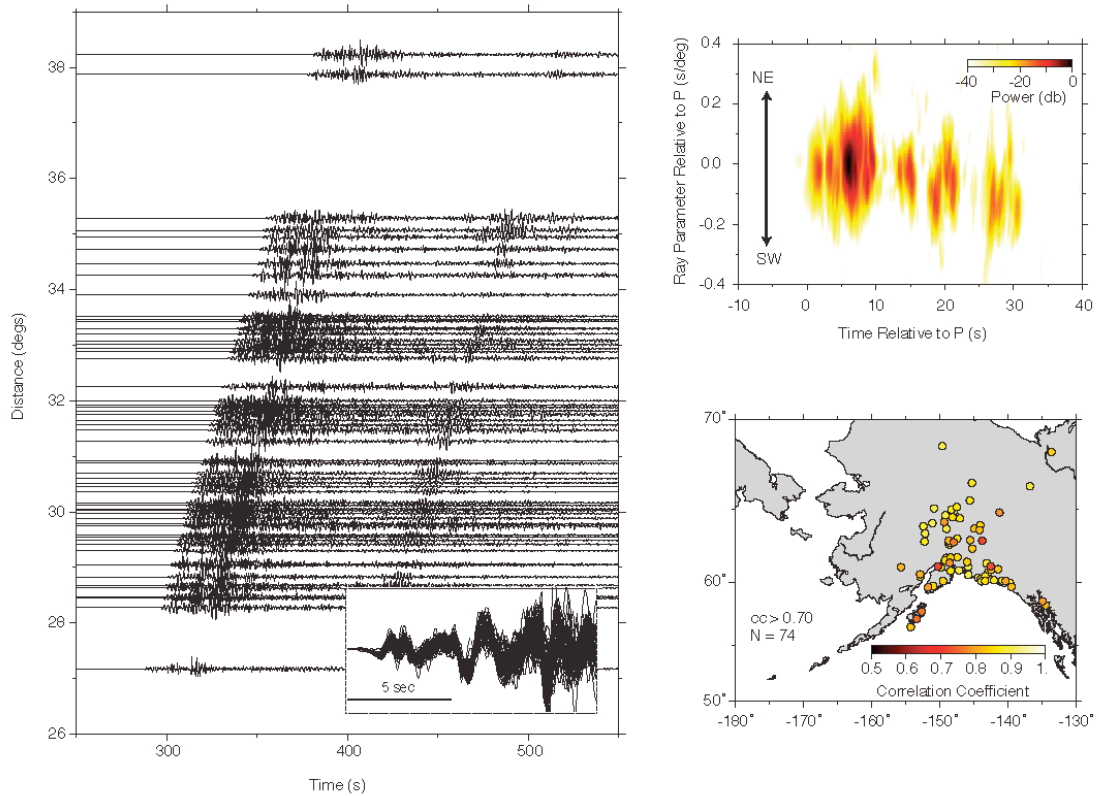
Fig. S5. Slowness variations for stations in Alaska. (a) The mainshock was well-recorded at seismic stations in Alaska, with. A profile of data is shown on the left, with the inset showing the well-correlated onset of the waveforms in the first second aligned by multi-channel correlations (the map at lower right shows the correlation coefficients for the aligned stations). The top right is a plot of travel-time ray parameter (slowness) as a function of time (vespagram). The decrease in ray parameter with time indicates that the source in rupturing away from the array (southward).
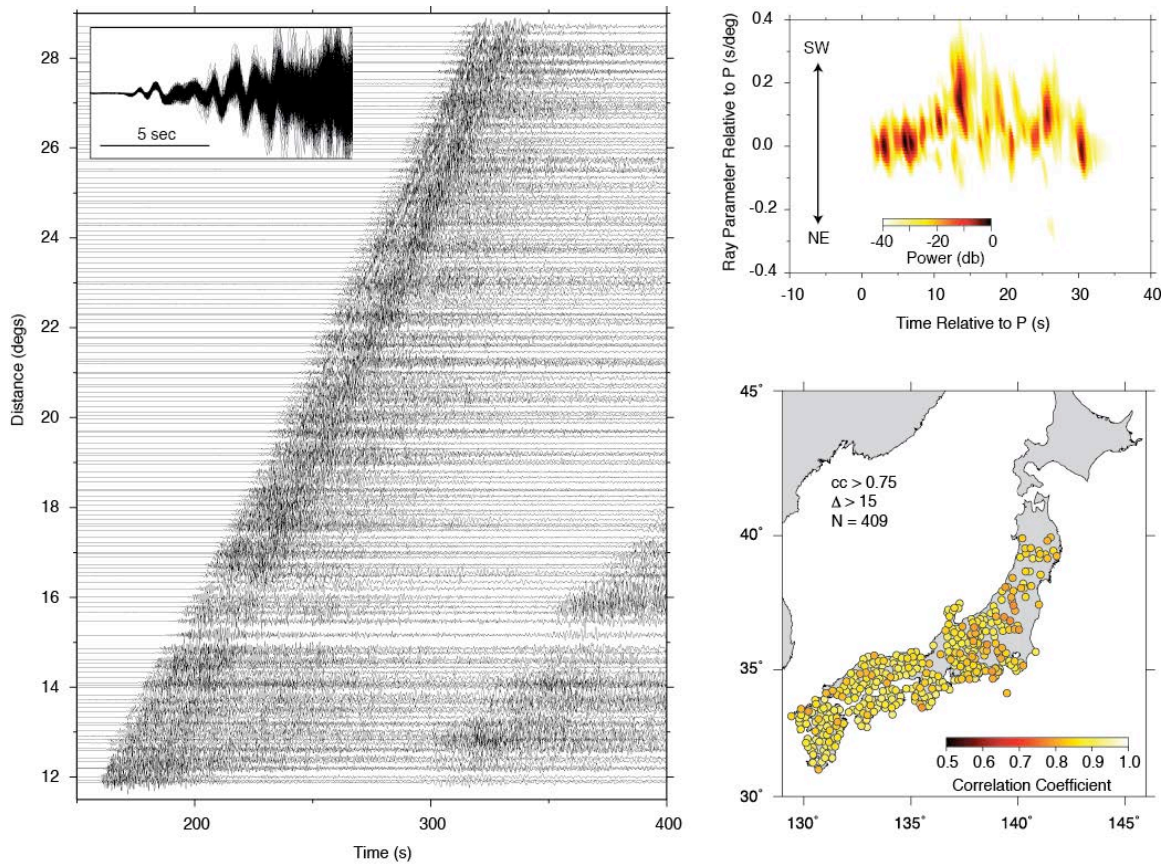
Fig. S6. Slowness variations for Hi-net stations in Japan. (a) The mainshock was well-recorded at short-period borehole stations across Japan in the Hi-net array. A profile of data is shown on the left, with the inset showing the highly correlated onset of the waveforms in the first second aligned by multi-channel correlations (the map at lower right shows the correlation coefficients for the aligned stations). The top right plot is a vespagram. The increase in ray parameter with time for the first 15 s of the waveform indicates that the source in rupturing toward the array (southward).
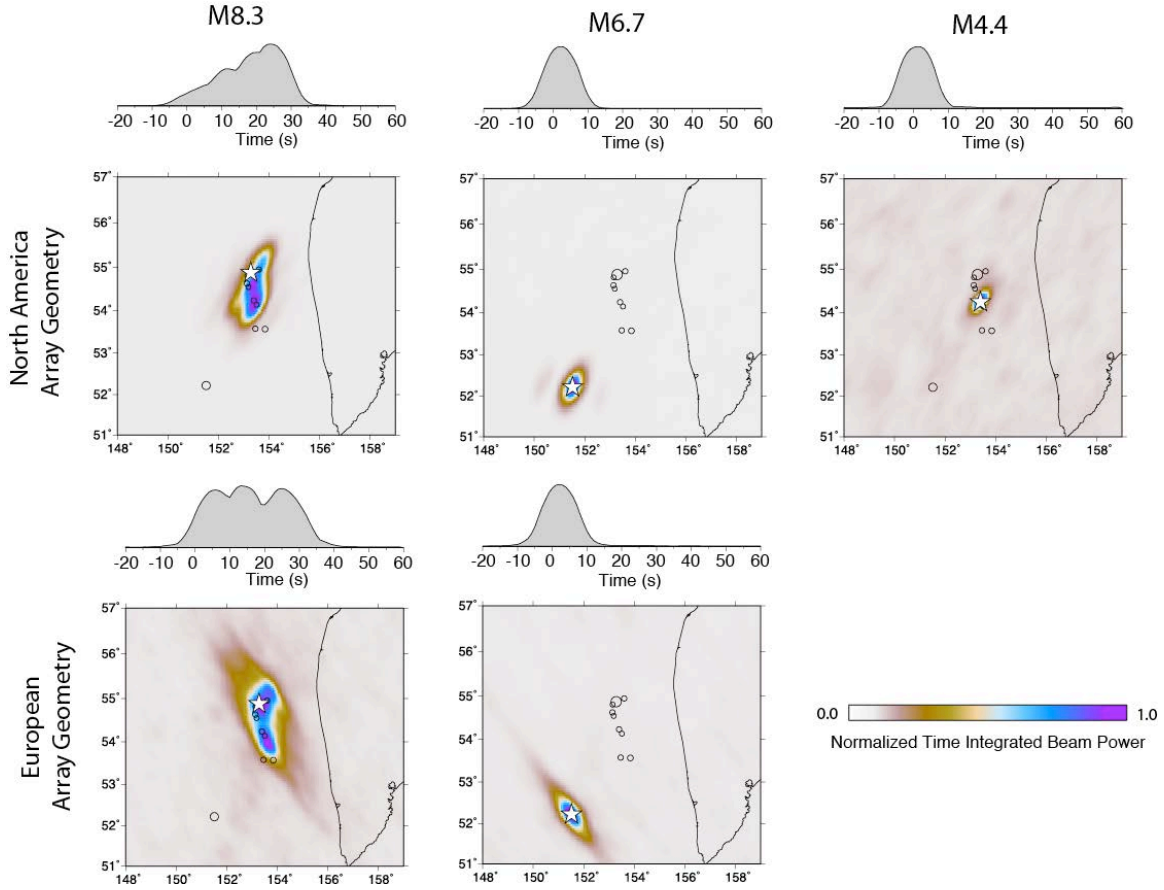
Fig. S7. Time-integrated plots of high frequency P wave back-projections for the mainshock and two aftershocks for data from North America and Europe stations. An evaluation of the network response artifacts in the back-projections for the M_w 8.3 mainshock is provided by back-projection of observations from the same stations for the M_w 6.7 aftershock and, for North America only, a m_b 4.4 aftershock. The two aftershocks should essentially be point-sources of energy due to having small spatial and temporal distributions of their energy release, and they are well imaged as spatially concentrated sources for data from both network configurations. The images with southern extension for the mainshock are thus reliable features of the finiteness, with any localized subevent pulses during the mainshock event being smeared out in the images to the same extent as for the aftershocks.
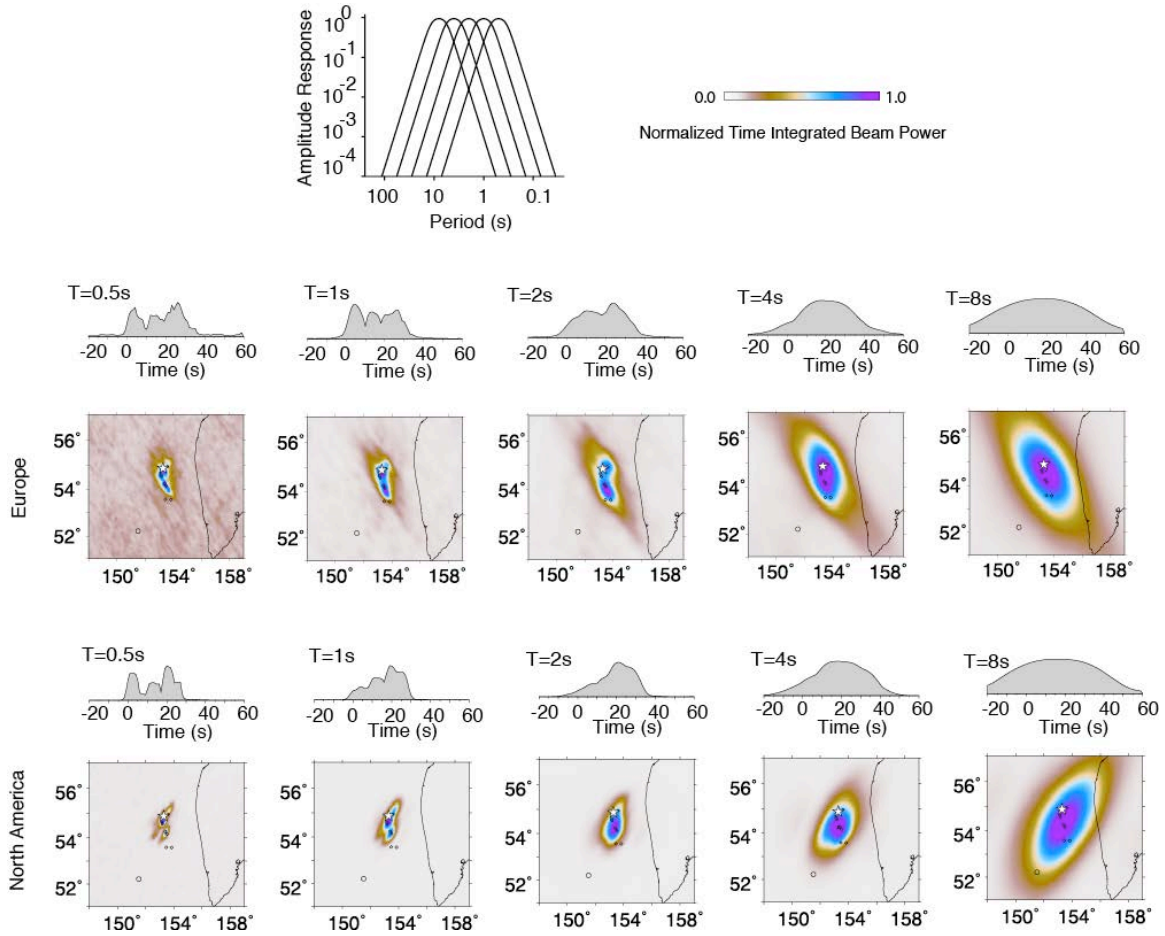
Fig. S8. Time-integrations of back-projections for a suite of narrow-band filtered P waves. The results for Europe and North American observations are shown. The narrowband filters are shown at the top left. The time-integrated back-projection for the P waves in each passband, aligned by the broadband signal correlations, are shown in the maps, with time-variation of peak image amplitude shown above each image. The decreasing temporal and spatial resolution with increasing period is a consequence of reduction of the move-out time lags for the finite-rupture relative to the dominant period of the signals.
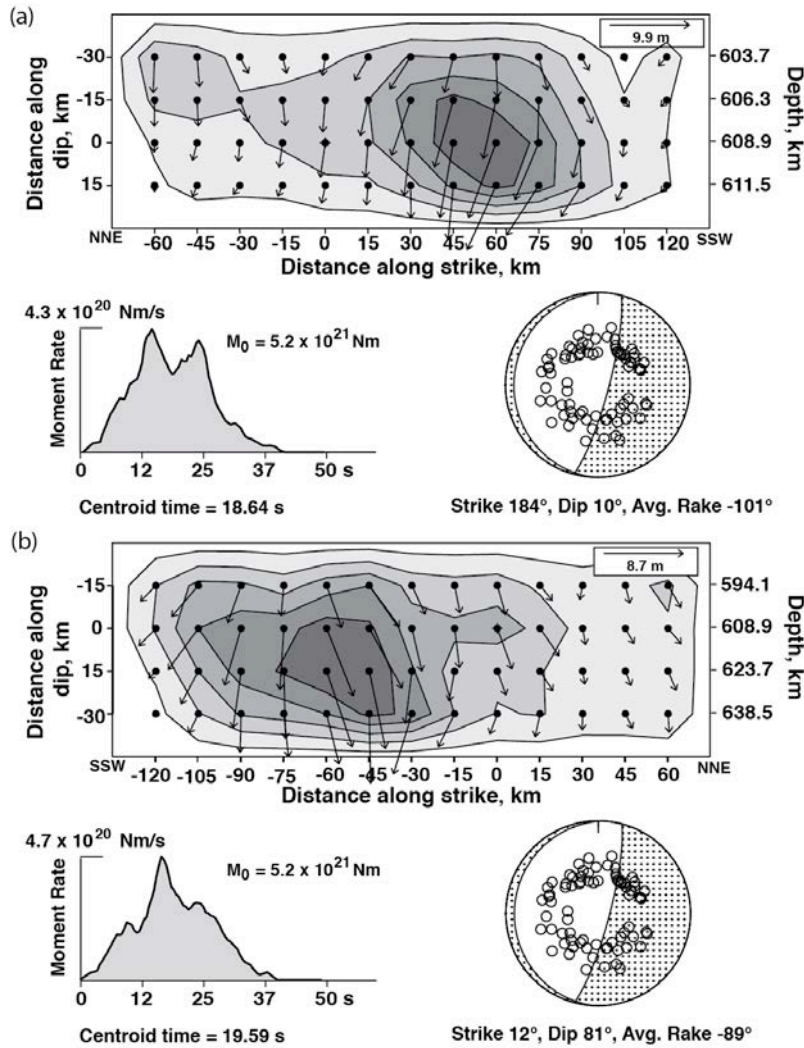
Fig. S9. The preferred rupture models. These models are for (a) the shallow dipping fault plane and (b) the steeply dipping fault plane. Both have a rupture velocity of 4.0 km/s, with the along-strike dimension being compatible with the back-projection images in Fig. S4, and the along-dip dimension being constrained so that the calculated stress drop for the average slip for subfaults with moment at least 15-20% of the largest subfault moment is 15 MPa, using the formula for a contained dip-slip fault with a width of 60 km. For this stress drop, the radiation efficiency is compatible with a Mode III crack with corresponding rupture velocity (Fig. 4). The upper figure in each part shows the slip model with vectors indicating the variable rake on the fault (motion of the upper block relative to the lower block) with slip contoured in m. The source moment rate function is shown at the lower left, and has a centroid time of 18.6 s, compatible with the W-phase inversion centroid time. The focal mechanism shows the faulting geometry and gives the average rake of the fault model (strike and dip are fixed), and the take-off angles of P waves used in each inversion are shown. The corresponding waveform matches for the model in (a) are in Fig. S10.
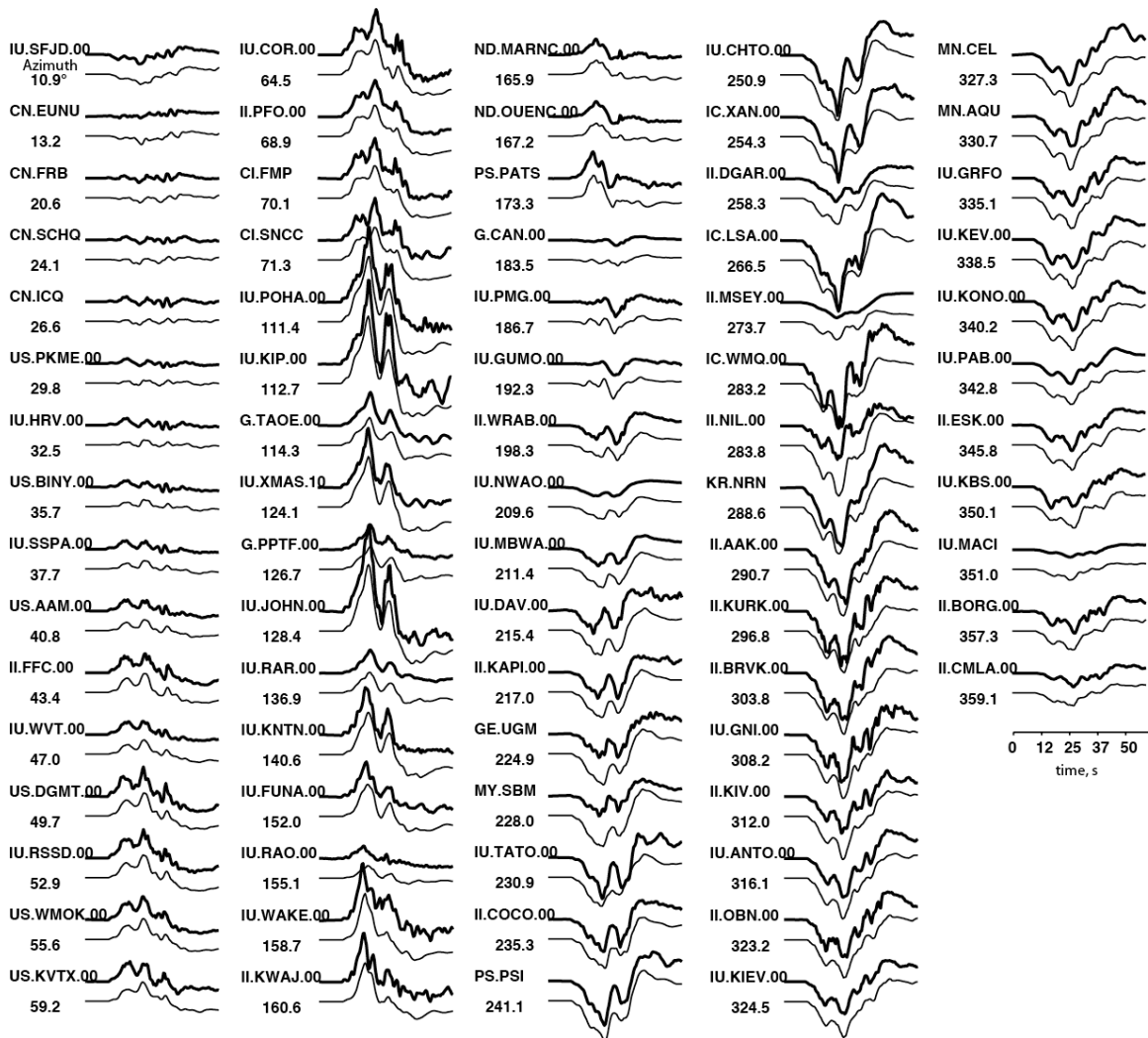
15

Fig. S10. P wave observations and predictions for the preferred shallow dipping model. Comparison of global teleseismic P wave observations (bold lines) and synthetics (light lines) for all data used in the finite-fault inversion in Fig.1 and Fig. S9a. Each station name and azimuth is given and all amplitudes are on a common scale. A 60 s time window with 10 s leader was used in the inversion.
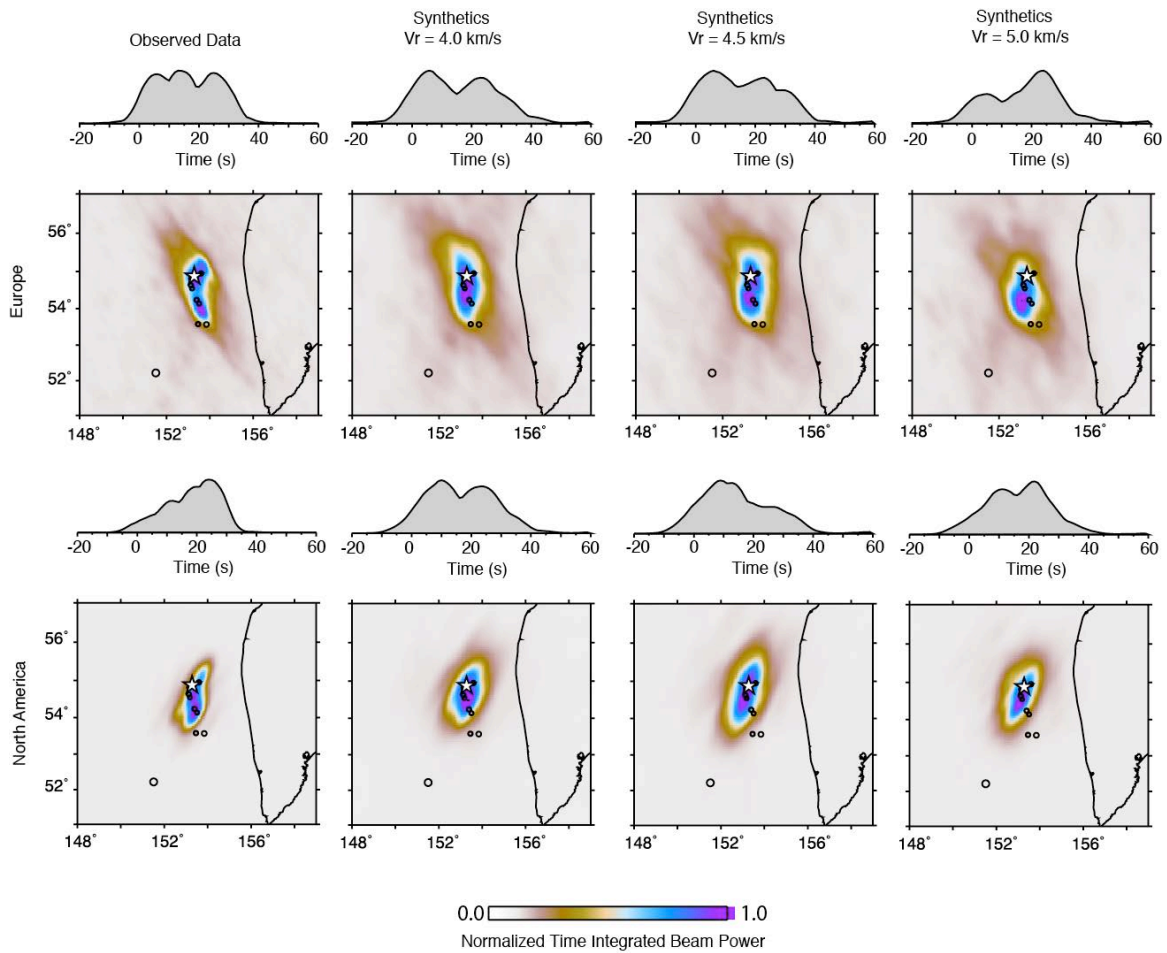
Fig. S11. Comparison of observed and synthetic back-projections. The time-integrated maps for back-projections of the data from Europe and North America (left column) are compared with back-projections for rupture models with varying rupture velocity that satisfy the radiation efficiency as shown in Fig. 4. The synthetics were made at the same stations and processed the same way as the data. The period range is 0.5-2.0 s. Models for the shallow-dipping fault plane (as in Fig. S9a) are shown Very similar comparisons are found for synthetics for models with the steeply dipping fault plane (as in Fig. S9b), with somewhat narrower features being imaged.
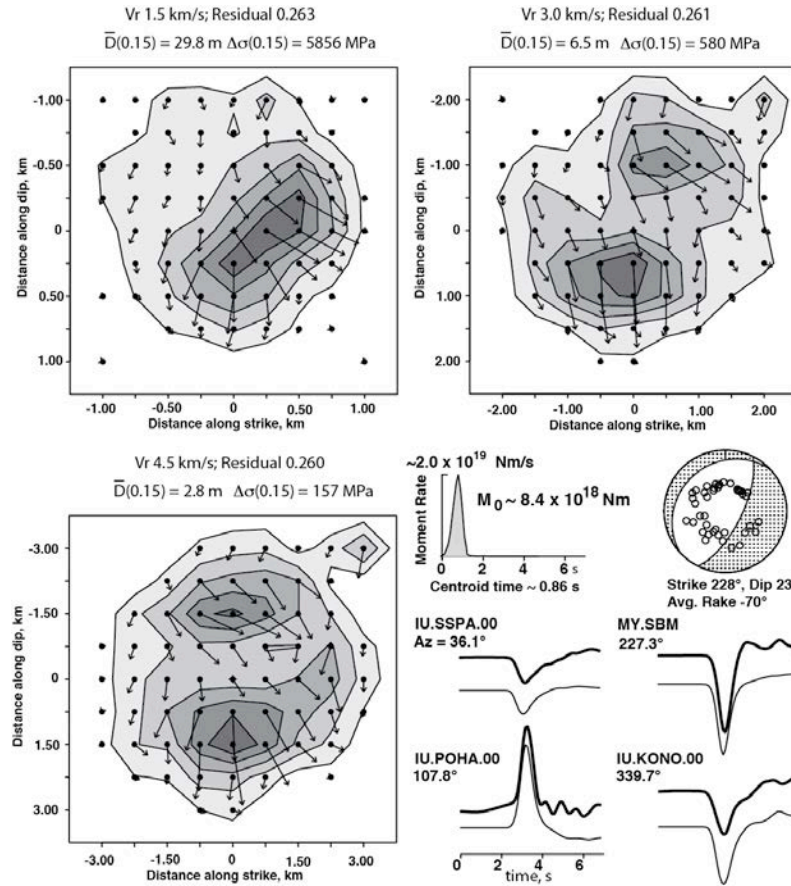
Fig. S12. Aftershock finite-fault models for varying rupture velocity. Slip distributions for three models with different constant rupture velocity with grid spacing scaling proportional to grid velocity. The strike is 228° and dip is 23° for all cases. Compact model grids are used, with the hypocenter located at the center of each grid. For small *Vr* the rupture is relatively circular, but as it increases the slip pattern develops two small patches. There is negligible difference in fit to the data for the different rupture models. For each model, the average displacement is computed for only those subfault sources with a seismic moment at least 15% as large as the largest sub-fault seismic moment and these values are given as D(0.15). Using the corresponding area of the remaining subfaults, a static stress drop is calculated using a circular rupture with radius matching the area of significant slip. There is about a factor of 37 range in stress drop estimate, and the stress drop is in the range 157 MPa to 5856 MPa. All of the inversions give similar source time functions, seismic moments and centroid times, with representative values being shown along with the average focal mechanism. Examples of waveform data (bold lines) and synthetics (thin lines) are shown, indicating the very short pulse of the teleseismic P wave signal, with some stations having minor broadening due to attenuation or slab diffraction. The energetic, short-duration impulse nature of the source made it a good empirical Green function event.
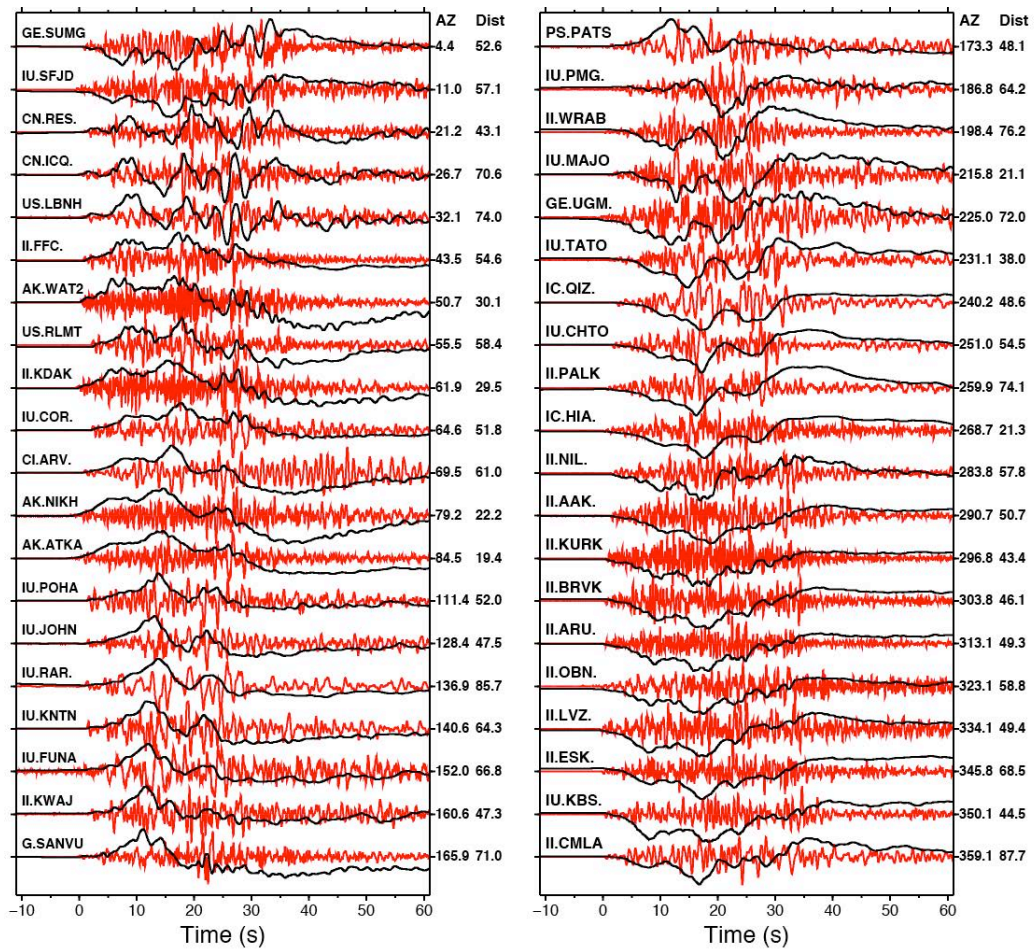
Fig. S13. Ground motion accelerations and displacements. Teleseismic P wave recordings from globally distributed broadband seismic stations for the 2013 Sea of Okhotsk event are shown, with the ground displacements given by the black lines and the corresponding ground accelerations given by the red lines. There is good correspondence between the overall temporal distribution of ground accelerations and the displacements (both are free of interference with surface reflections), and this supports use of short-period back-projection as a guide on the rupture kinematics.

Movie S1. Animation of back-projections of 0.5-2.0 Hz P waves for North America (NA) and European (EU) stations for the 2013 Okhotsk mainshock. The short-period P wave beam power stacked on a horizontal grid of possible source locations is shown as a function of time for the NA (left) and EU (right) stations distributions shown in Fig. S4. The color scale ranges from zero beam power (white) to unity normalized beam power (purple). The peak beam power at each time increment is tracked at the top with the sliding red bar indicating the time. This produces an approximation of the short-period energy radiation time history toward each network.